

## Network of Topological Nodal Planes, Multifold Degeneracies, and Weyl Points in CoSi

Nico Huber<sup>1</sup>, Kirill Alpin<sup>2</sup>, Grace L. Causer<sup>1</sup>, Lukas Worch<sup>1</sup>, Andreas Bauer<sup>1</sup>, Georg Benka<sup>1</sup>,  
Moritz M. Hirschmann<sup>2</sup>, Andreas P. Schnyder<sup>2</sup>, Christian Pfleiderer<sup>1,3,4</sup> and Marc A. Wilde<sup>1,\*</sup>

<sup>1</sup>Physik Department, Technische Universität München, D-85748 Garching, Germany

<sup>2</sup>Max-Planck-Institute for Solid State Research, Heisenbergstrasse 1, D-70569 Stuttgart, Germany

<sup>3</sup>MCQST, Technische Universität München, D-85748 Garching, Germany

<sup>4</sup>Centre for Quantum Engineering (ZQE), Technische Universität München, D-85748 Garching, Germany



(Received 6 July 2021; revised 26 January 2022; accepted 24 May 2022; published 6 July 2022)

We showcase the importance of global band topology in a study of the Weyl semimetal CoSi as a representative of chiral space group (SG) 198. We identify a network of band crossings comprising topological nodal planes, multifold degeneracies, and Weyl points consistent with the fermion doubling theorem. To confirm these findings, we combined the general analysis of the band topology of SG 198 with Shubnikov–de Haas oscillations and material-specific calculations of the electronic structure and Berry curvature. The observation of two nearly dispersionless Shubnikov–de Haas frequency branches provides unambiguous evidence of four Fermi surface sheets at the  $R$  point that reflect the symmetry-enforced orthogonality of the underlying wave functions at the intersections with the nodal planes. Hence, irrespective of the spin-orbit coupling strength, SG 198 features always six- and fourfold degenerate crossings at  $R$  and  $\Gamma$  that are intimately connected to the topological charges distributed across the network.

DOI: [10.1103/PhysRevLett.129.026401](https://doi.org/10.1103/PhysRevLett.129.026401)

In recent years the identification of nontrivial topological quasiparticles (TQPs) in solids attracts great interest in the context of spintronics and quantum technological applications. Contributions of such topological quasiparticles in the physical properties are expected to scale with the Berry curvature of the bands, the inverse energy difference between the band crossings and the Fermi level, and the separation of corresponding sources and sinks of Berry curvature in  $k$  space. However, to account for these phenomena, knowledge of the distribution of topological charges across the entire band structure around the Fermi level is required.

The need for determining the global band topology may be highlighted in terms of maximally large Chern numbers in nonmagnetic chiral materials crystallizing in SG 198, such as CoSi, RhSi, and PdGa [1–6], recently inferred from the observation of Fermi arcs [4–7] and quasiparticle interference patterns [8]. Based on the bulk-boundary correspondence and *ab initio* calculations, these observations were attributed to degeneracies at the  $\Gamma$  and  $R$  point, where the corresponding charges were believed to satisfy the fermion doubling theorem (FDT) between them [9,16], but where the global band topology had not been

determined. However, the discovery of symmetry-enforced topological nodal planes (NPs) in the ferromagnetic state of MnSi [17], described by magnetic subgroups of SG 198 suggests that this picture may be incomplete, raising questions for (i) the existence of topological NPs in SG 198, (ii) whether the analysis of the band topology and the Berry curvature for specific points reported so far is sufficient for an assessment of their impact on the physical properties, and (iii) whether strongly simplified Hamiltonians of the TQPs as inspired by high-energy physics [1] are justified [3].

Further, when spin-orbit coupling (SOC) is strong as in PdGa, spin degeneracies are lifted, leading to fourfold and twofold points at  $\Gamma$  and a sixfold point at  $R$  [7]. In contrast, it has been argued that SOC may be ignored in the light transition metal silicides CoSi and RhSi such that all bands are spin-degenerate, leading to a threefold point at  $\Gamma$  and a fourfold point at  $R$  [18]. In fact, scanning tunneling microscopy studies in CoSi suggest a SOC as large as 25 to 35 meV [8], while conflicting interpretations of quantum oscillations in CoSi inferred a SOC as low as 1 meV [19–21]. This raises the additional question of how to reconcile the topological properties of SG 198 with SOC and NPs, being dictated by fundamental quantum theory and crystal symmetry.

To resolve these questions requires determination of the complete set of topological charges, starting with a general symmetry analysis. As SG 198 is chiral with three twofold screw rotations along the three main axes, we note that any band structure in this SG contains NPs on the three

Published by the American Physical Society under the terms of the [Creative Commons Attribution 4.0 International license](https://creativecommons.org/licenses/by/4.0/). Further distribution of this work must maintain attribution to the author(s) and the published article's title, journal citation, and DOI.

Brillouin zone (BZ) boundaries  $k_{x,y,z} = \pm\pi$ . This trio of NPs can carry a finite topological charge that is protected by the screw rotations combined with time-reversal symmetry [17,22,23]. Inferring the existence of band crossings on high-symmetry points and lines from the dimensionality of the irreps of the little groups and their compatibility relations, we performed a general band topology analysis and determined the main aspects of NPs in SG 198 (see Supplemental Material (SM) [9] for details). For instance, with SOC there can be twofold and fourfold degeneracies at  $\Gamma$ , while on the  $\Gamma$ -X path there are symmetry-enforced, movable Weyl crossings. With SOC the pinned crossings at  $\Gamma$  enforce a topological charge of the NPs. Finally, the multiplicity of accidental crossing points at and away from high-symmetry lines or planes is independent of SOC, and the Chern number of symmetry-related Weyl points is always the same since SG 198 does not contain inversion or mirror symmetries. Taken together, a symmetry-enforced topological charge of the NPs must be *odd*. This shows that earlier assessments were incomplete [1–7].

To confirm these general findings we studied CoSi, calculating the band structure and Fermi surface (FS) in density functional theory (DFT) using WIEN2K [24] and QUANTUM ESPRESSO [25,26] within the generalized gradient approximation [27]. We then determined the band topology in addition to the topological charges of the trio of NPs, computing the Berry curvature from the DFT wave functions by means of an algorithm based on Wilson loops we developed for this purpose [28–31] (for details, see SM [9]).

In the following we denote the Chern number,  $\nu$ , and the multiplicity,  $l$ , of band crossings with and without SOC by  $\nu_A^n$ ,  $l_A^n$  and  $\tilde{\nu}_A^n$ ,  $\tilde{l}_A^n$ , respectively [9]. Here,  $A$  denotes the location in the BZ and  $n$  designates the index of the energetically lower band (or band pair when the crossing is located on a NP) that participates in the degeneracy going from low to high energies starting above the global band gap at  $\sim -0.5$  eV. While we do not denote the spin degeneracy explicitly when labeling bands, we include it in the Chern numbers.

Summarized in Fig. 1 are the band structures of CoSi without and with SOC as well as illustrations of key results of our band topology analysis. Cyan shading highlights the NPs. Bands intersecting with the NPs are marked in color. Topological point crossings are marked by colored circles. Curly brackets denote all well-defined Chern numbers of the crossing bands in ascending order in energy. Fermi surface degeneracies (FSDs) and topological protectorates (TPs) [17] are marked by triangles. Here, the expression “topological protectorates” refers to intersections of FS sheets with NPs that carry a nonzero topological charge. The expression was introduced in Ref. [17] to highlight that TPs guarantee that topological properties are pinned to  $E_F$ , independent of material-specific details.

Consistent with the underlying symmetries, the band structure of CoSi exhibits NPs on the three BZ boundaries regardless of SOC. Without SOC all bands are

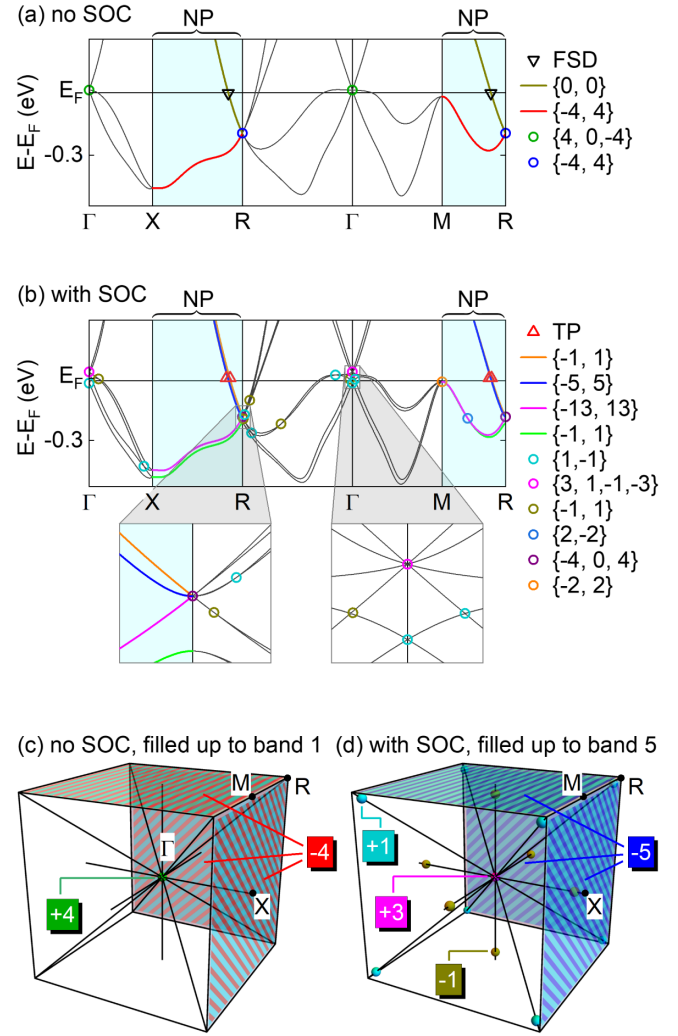


FIG. 1. Electronic band structure of CoSi. See text for details of notation. (a) Band structure without SOC. (b) Band structure with SOC. Insets: Enlarged views around  $R$  and  $\Gamma$ . (c),(d) Illustration of the FDT for selected band fillings. No SOC and filling up to band 1 yields a charge of +4 at  $\Gamma$  (green) compensated by the trio of NPs with charge  $-4$  (red/cyan). With SOC and filling up to band 5 the bulk crossing points carry a net charge of +5, taking into account their multiplicities, which is compensated by the trio of NPs with charge  $-5$  (blue/cyan).

spin-degenerate [Fig. 1(a)], and there are two spin-degenerate trios of NPs close to the Fermi energy  $E_F$ , where the topological charges for each of the crossings add to zero in accordance with the FDT. With SOC the spin degeneracy is lifted [Fig. 1(b)] and the two trios of NPs split into four trios and the corresponding crossings at  $\Gamma$  are forced to carry odd topological charges [1,3]. For these odd band fillings  $n$  the charges at  $\Gamma$  can only be compensated by the trios of NPs, as all other crossings (accidental or enforced) sum to an even number [9,17]. Thus, with SOC the two NP trios crossing  $E_F$  form TPs.

To determine the relationship between the different topological charges, we analyzed the band structure of

CoSi systematically for different band fillings. Without SOC we found that the NPs are not forced by symmetry to carry a charge. In contrast, with SOC all NPs are forced to carry topological charges by symmetry.

Two selected band fillings nicely illustrate this situation (for all other fillings see SM [9]). First, without SOC and the first band being filled, the trio of NPs that is lower in energy, marked in red/cyan in Fig. 1(c), supports a charge of  $\nu_{\text{npt}}^1 = -4$  that compensates the charge of  $\nu_{\Gamma}^1 = +4$  of the threefold point at  $\Gamma$  (green), in agreement with the FDT [16]. The upper trio of NPs, in contrast, has charge zero, since the Chern numbers at  $\Gamma$  given by  $(\nu_{\Gamma}^1, \nu_{\Gamma}^2, \nu_{\Gamma}^3) = \{4, 0, -4\}$  add up to zero [green circle in Fig. 1(a)], when the lowest three bands are filled. Second, when taking into account SOC, the situation changes fundamentally as illustrated in Fig. 1(d) for a filling up to band 5. Here, we find at  $\Gamma$  a total charge  $\nu_{\Gamma}^3 + \nu_{\Gamma}^4 + \nu_{\Gamma}^5 = +3$ . On the  $\Gamma$ -X line there is a movable Weyl point with charge  $\nu_{\Gamma X}^5 = -1$  and multiplicity  $l_{\Gamma X}^5 = 6$ , resulting in a charge  $l_{\Gamma X}^5 \nu_{\Gamma X}^5 = -6$ . On the  $\Gamma$ -R line there is a crossing,  $\nu_{\Gamma R}^5 = +1$  very close to R, contributing a total charge  $l_{\Gamma R}^5 \nu_{\Gamma R}^5 = 8$ . Since an odd number of bands is filled, the point crossings at M and R within the NP do not contribute any charge. Hence, according to the FDT the NP must compensate these charges, i.e.,  $\nu_{\text{npt}}^5 = -\nu_{\Gamma}^3 - \nu_{\Gamma}^4 - \nu_{\Gamma}^5 - 6\nu_{\Gamma X}^5 - 8\nu_{\Gamma R}^5 = -3 + 6 - 8 = -5$ . This result is also obtained in direct numerical calculations [9], indicating the absence of additional uncompensated Weyl points at generic positions.

To prove the existence of NPs experimentally, we measured the quantum oscillations arising from the FS sheets centered at the R point as these sheets intersect with the NPs (Fig. 2) [19–21]. Here, FSDs and TPs denote the location of FS degeneracies (black line) and topological protectorates (red line), respectively, and the numbers denote the octants of the FS sheets facing the observer. A constant length has been subtracted from the distance between R and the FS contour for better visibility of the different shapes. The predicted SOC splitting at  $E_F$  around R is small,  $\sim 15$  meV, for low-symmetry directions. This corresponds to a  $k$ -space distance of the FS sheets of about  $\sim 0.7\%$  of a reciprocal lattice vector, which may be readily resolved in quantum oscillations.

Without SOC two spin-degenerate sheets are expected [Figs. 2(a1)–2(a3)], which exhibit topologically trivial FSDs on the NPs [Fig. 2(a1)]. Ignoring the NPs [Fig. 2(a2)], the extremal cross-sectional areas are identical for  $B \parallel [100]$ , resulting in a single oscillation frequency [cf. Fig. 4(a)]. Note that this is a ‘‘Gedankenexperiment’’ assuming that individual bands as sorted by their energy eigenvalues are not connected at the NPs, which we subsequently falsify by showing the contradiction to experiment. In comparison, for arbitrary directions the FS cross sections are different [Fig. 2(a2)] and two dispersive frequency branches are expected [cf. Fig. 4(a)]. Considering now the NPs [Fig. 2(a3)], the band connectivity changes such that (space-) diagonally

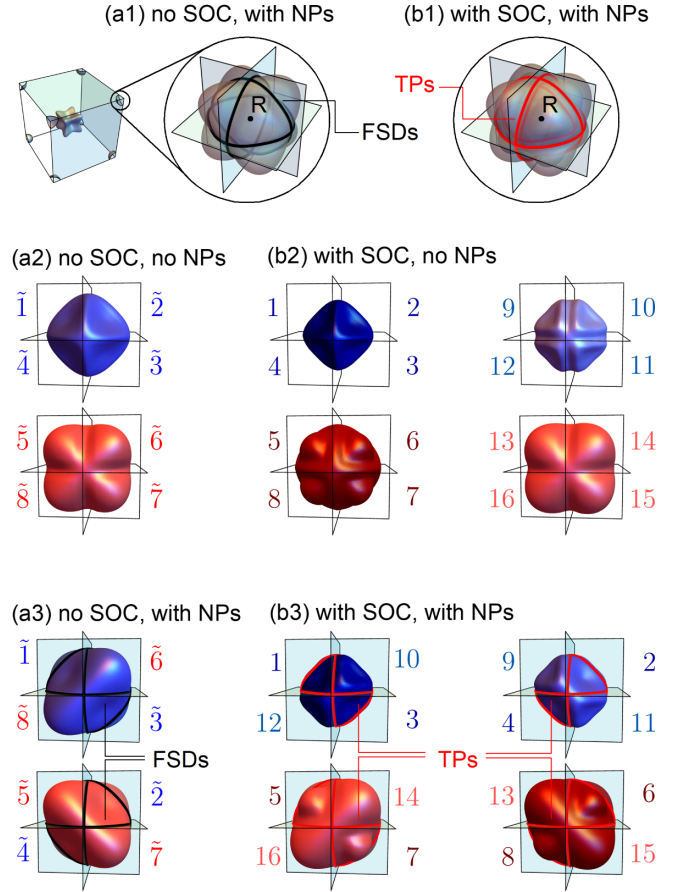


FIG. 2. Effect of SOC and NPs on the FS sheets at the R point. See text for details of notation. (a1),(b1) FS sheets at the R point and splitting without and with SOC. (a2),(a3) FS sheets at the R point without SOC. Two spin-degenerate sheets are expected. NPs alter the band connectivity such that diagonally located octants combine to form the FS sheets. (b2),(b3) FS sheets at the R point with SOC. Effect of the NPs is the same as in (a3).

located octants are recombined, i.e., sectors  $\tilde{1}$  and  $\tilde{3}$  in Fig. 2(a2) combine with  $\tilde{6}$  and  $\tilde{8}$  in Fig. 2(a2) (and analogously for the octants facing away from the observer) to form the blue FS sheet shown in Fig. 2(a3). Vice versa, sectors  $\tilde{2}$ ,  $\tilde{4}$ ,  $\tilde{5}$ , and  $\tilde{7}$  form the red FS sheet shown in Fig. 2(a3). The extremal cross sections of the reconstructed FS sheets are essentially identical regardless of orientation, resulting in a single almost dispersionless frequency branch even though two FS sheets contribute [cf. Fig. 4(c)]. Further, the band connectivity suppresses transitions between different sheets and thus additional branches.

With SOC the spin degeneracy is lifted resulting in four FS sheets [Figs. 2(b1)–2(b3)]. The analysis of the band topology reported above establishes TPs (red lines). The effects of the NPs are identical to the FS sheets without SOC. Because of the band connectivities at the NPs, the four FS sheets reduce to two pairs with essentially identical cross sections regardless of orientation [Fig. 2(b3)]. Thus, two frequency branches with low dispersion are expected

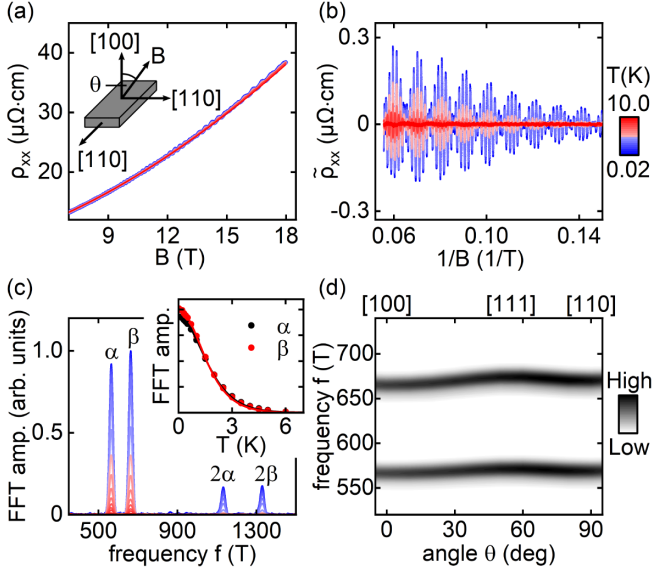


FIG. 3. Typical SdH data. (a) Magnetoresistance  $\rho_{xx}(B)$ ; Inset: experimental geometry using cubic equivalent directions. (b) Oscillatory part of the resistivity  $\tilde{\rho}_{xx}(1/B)$  for selected temperatures. (c) FFTs of  $\tilde{\rho}_{xx}(1/B)$ . Two frequencies  $f_\alpha = 565$  T and  $f_\beta = 663$  T and their harmonics are resolved. Inset: Lifshitz-Kosevich behavior of the FFT amplitudes, yielding effective masses  $m_\alpha = 0.90 m_e$  and  $m_\beta = 0.95 m_e$ . (d) FFT amplitude versus frequency and field direction  $\theta$ . Both SdH branches exhibit a very low dispersion.

even though four FS sheets contribute [see Fig. 4(d)] This picture gets modified when additionally taking into account magnetic breakdown, which further decreases the angular dispersion of the two branches with the highest weight.

To confirm our predictions for the FS sheets centered at  $R$  we measured the Shubnikov–de Haas (SdH) effect. Our data are in excellent agreement with the literature [19–21,32]. For details on the experimental methods, see SM [9]. As illustrated in Fig. 3(a), the resistivity  $\rho_{xx}$  exhibits pronounced quantum oscillations for magnetic fields  $B \parallel [100]$  exceeding  $\sim 6$  T on a monotonically increasing background, where the oscillatory component of the signal is shown in Fig. 3(b). Fast Fourier transforms (FFTs) were calculated using a Hamming window, where typical FFT spectra are shown in Fig. 3(c).

Two frequencies,  $f_\alpha = 565$  T and  $f_\beta = 663$  T, and their higher harmonics could be resolved. Based on close inspection of the higher harmonics observed in samples of different quality, we conclude that asymmetries of the FFT peaks reported previously are not intrinsic (see SM [9] for details). The temperature dependence of the FFT amplitude was analyzed within the Lifshitz-Kosevich formalism [33], yielding effective masses  $m_\alpha = 0.90 m_e$  and  $m_\beta = 0.95 m_e$  [inset of Fig. 3(c)]. The angular dispersion of the SdH branches is shown in Fig. 3(d), where the strength of the shading reflects the FFT amplitude. The variation of frequency with  $\theta$  was very low around  $\sim 5$  T and  $\sim 10$  T for  $f_\alpha$  and  $f_\beta$ , respectively.

For the interpretation of our data we assume a semiclassical quasiparticle motion and magnetic breakdown according to Chambers’ formula [9,33]. Shown in Fig. 4 are the cyclotron orbits for selected field orientations and comparisons of the experimental frequency branches (gray scale) with the calculated behaviors (colored lines) [Figs. 3(a)–3(d)]. We note that orbits enclosing the small areas in between adjacent large orbits are semiclassically forbidden, because an electron would have to travel on trajectories opposing the Lorentz force as indicated by the arrows.

Without SOC and NPs, representing the interpretation in Refs. [19,20], there are two spin-degenerate bands crossing  $E_F$  near  $R$ . For  $B \parallel [100]$  the two extremal orbits coincide [Fig. 4(a)], resulting in a single SdH frequency. A tiny splitting of the upper branch close to  $[100]$ , reflecting the constrictions of the red FS sheet in Fig. 2(a), vanishes quickly under field rotation, whereas the main branch splits into a dispersive inner and outer orbit in stark contrast with experiment.

Further, neglecting SOC but taking into account the band connectivity due to the NPs [Fig. 4(b)], the extremal cross

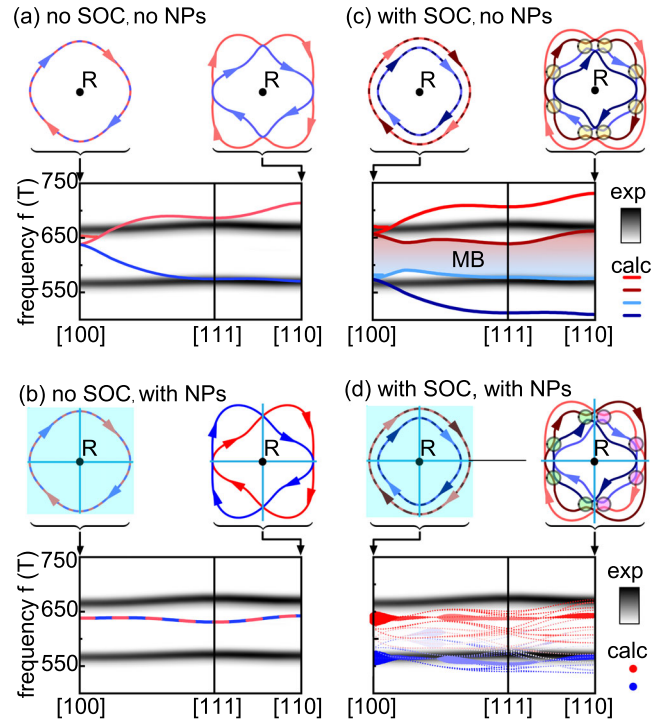


FIG. 4. Comparison of experimental SdH branches (gray scale) and calculated branches (color). From the shapes of extremal orbits for  $B \parallel [100]$  and  $B \parallel [110]$ , an  $R$ -centered circle was subtracted for better visibility. Magnetic breakdown junctions are marked by colored circles. (a) Without SOC and without NPs. (b) With NPs (cyan) and without SOC. (c) With SOC and without NPs. Shaded area reflects up to 8192 partly degenerate breakdown branches. (d) With SOC and with NPs. Breakdown branches are calculated explicitly, with symbol size reflecting the orbit probability resulting in two strong almost dispersionless branches.

sections of the two FS sheets will be the same, resulting in a single SdH frequency [see Fig. 4(b)]. Upon field rotation the bands continue to cross at the NPs with orthogonal wave functions and thus without interaction, giving rise to a *single* nondispersive SdH branch, in contrast with experiment.

Shown in Fig. 4(c) is the behavior when including SOC but neglecting the NPs as proposed in Ref. [21]. Again, a small branch splitting is expected close to [100]. Because of SOC, four distinct FS sheets would exist around  $R$  with pairwise degenerate extremal cross sections for  $B\parallel[100]$  that split into four branches under field rotation. Since the extremal orbits on the intermediate sheets 2 and 3 would come close to each other at up to 12 breakdown junctions (yellow circles), up to 8192 (highly degenerate) breakdown branches are expected as indicated by the shading between branches 2 and 3. None of this is observed experimentally.

The presence of both SOC and NPs are, finally, shown in Fig. 4(d). Since the spin degeneracy is lifted and the extremal orbits reside on a NP (cyan) for  $B\parallel[100]$ , two extremal cross sections and thus two SdH frequencies are expected. Under field rotation these split into four orbits that intersect at the NPs and remain pairwise-degenerate. Magnetic breakdown occurs at the same junctions as in Fig. 4(c). However, due to the band connectivities only up to 6 breakdown junctions are expected for each pair of orbits [Fig. 4(d)]. Calculating the frequency spectra in DFT [9], we find two dominant branches with a high probability as indicated by the symbol size with a difference between 80 T and 90 T and a very low dispersion of  $\sim 10$  T, as well as a tiny probability for other breakdown branches, all in excellent agreement with experiment.

Taken together, we demonstrated the importance of a general analysis of the global band topology for the example of SG 198, focusing on CoSi [17]. The SdH frequencies associated with FS sheets at the  $R$  point we observed in CoSi provide unambiguous evidence of a sixfold degeneracy at  $R$  even for weak SOC, implying a fourfold degeneracy at  $\Gamma$ . [4–6,8,19–21]. These degeneracies are part of a topological network comprising, in addition, the topological NPs, the fourfold crossings at  $M$ , the enforced Weyl points on screw rotation axes, as well as accidental Weyl points at generic positions in the BZ, in combination satisfying the FDT [9,16]. Although the NPs do not give rise to additional Fermi arcs at the surface, they will contribute substantially to the bulk topological responses, such as spin anomalous Hall currents and nonlinear optical properties. Moreover, in the light of our findings it seems difficult to justify the use of strongly simplified Hamiltonians of TQPs in analogy to particle physics.

Since our analysis is based on symmetry, it is also applicable to other nonmagnetic representatives of SG 198, such as PdGa, and can be generalized straightforwardly to other chiral or noncentrosymmetric SGs as well as other excitations such as phonons and magnons. This highlights

the need for a global assessment of the topological charges beyond isolated degeneracies for any material.

We wish to thank J. Knolle and A. Rosch for discussions. M. A. W., A. B., and C. P. were supported by the DFG in the framework of TRR80 (project E1 and E3, project id 107745057), SPP 2137 (Skyrmionics) under grant no. PF393/19 (project id 403191981), DFG-GACR project WI 3320/3-1, ERC Advanced grants no. 291079 (TOPFIT) and 788031 (ExQuiSid), and Germany's excellence strategy EXC-2111 390814868. A. P. S. thanks the Max Planck-UBC-UTokyo Center for Quantum Materials for support.

N. H. and K. A. contributed equally to this work.

*Note added.*—We recently became aware of Refs. [34,35], where topological charges of nodal planes are discussed, albeit with an erroneous double counting in Ref. [35].

---

\*Corresponding author.  
mwilde@ph.tum.de

- [1] P. Tang, Q. Zhou, and S.-C. Zhang, Multiple Types of Topological Fermions in Transition Metal Silicides, *Phys. Rev. Lett.* **119**, 206402 (2017).
- [2] G. Chang, S.-Y. Xu, B. J. Wieder, D. S. Sanchez, S.-M. Huang, I. Belopolski, T.-R. Chang, S. Zhang, A. Bansil, H. Lin, and M. Z. Hasan, Unconventional Chiral Fermions and Large Topological Fermi Arcs in RhSi, *Phys. Rev. Lett.* **119**, 206401 (2017).
- [3] D. A. Pshenay-Severin, Y. V. Ivanov, A. A. Burkov, and A. T. Burkov, Band structure and unconventional electronic topology of CoSi, *J. Phys. Condens. Matter* **30**, 135501 (2018).
- [4] Z. Rao, H. Li, T. Zhang, S. Tian, C. Li, B. Fu, C. Tang, L. Wang, Z. Li, W. Fan, J. Li, Y. Huang, Z. Liu, Y. Long, C. Fang, H. Weng, Y. Shi, H. Lei, Y. Sun, T. Qian, and H. Ding, Observation of unconventional chiral fermions with long Fermi arcs in CoSi, *Nature (London)* **567**, 496 (2019).
- [5] D. S. Sanchez *et al.*, Topological chiral crystals with helicoid-arc quantum states, *Nature (London)* **567**, 500 (2019).
- [6] D. Takane, Z. Wang, S. Souma, K. Nakayama, T. Nakamura, H. Oinuma, Y. Nakata, H. Iwasawa, C. Cacho, T. Kim, K. Horiba, H. Kumigashira, T. Takahashi, Y. Ando, and T. Sato, Observation of Chiral Fermions with a Large Topological Charge and Associated Fermi-Arc Surface States in CoSi, *Phys. Rev. Lett.* **122**, 076402 (2019).
- [7] N. B. M. Schröter, S. Stolz, K. Manna, F. de Juan, M. G. Vergniory, J. A. Krieger, D. Pei, T. Schmitt, P. Dudin, T. K. Kim, C. Cacho, B. Bradlyn, H. Borrmann, M. Schmidt, R. Widmer, V. N. Strocov, and C. Felser, Observation and control of maximal Chern numbers in a chiral topological semimetal, *Science* **369**, 179 (2020).
- [8] Q.-Q. Yuan, L. Zhou, Z.-C. Rao, S. Tian, W.-M. Zhao, C.-L. Xue, Y. Liu, T. Zhang, C.-Y. Tang, Z.-Q. Shi, Z.-Y. Jia, H. Weng, H. Ding, Y.-J. Sun, H. Lei, and S.-C. Li, Quasiparticle interference evidence of the topological Fermi arc

- states in chiral fermionic semimetal CoSi, *Sci. Adv.* **5**, eaaw9485 (2019).
- [9] See Supplemental Material at <http://link.aps.org/supplemental/10.1103/PhysRevLett.129.026401>, which includes Refs. [10–15], for a description of the DFT methods, a symmetry analysis of SG 198, the band structure topology of CoSi with and without SOC, generic tight-binding models for SG 198, as well as details of the experimental methods, the data analysis, and a specific comparison of our Shubnikov-de Haas spectra with the literature.
- [10] R. Sakuma, Symmetry-adapted Wannier functions in the maximal localization procedure, *Phys. Rev. B* **87**, 235109 (2013).
- [11] D. Gresch, G. Autès, O.V. Yazyev, M. Troyer, D. Vanderbilt, B.A. Bernevig, and A.A. Soluyanov, Z2Pack: Numerical implementation of hybrid Wannier centers for identifying topological materials, *Phys. Rev. B* **95**, 075146 (2017).
- [12] B. Bradlyn, L. Elcoro, J. Cano, M.G. Vergniory, Z. Wang, C. Felser, M.I. Aroyo, and B.A. Bernevig, Topological quantum chemistry, *Nature (London)* **547**, 298 (2017).
- [13] S.S. Tsirkin, I. Souza, and D. Vanderbilt, Composite Weyl nodes stabilized by screw symmetry with and without time-reversal invariance, *Phys. Rev. B* **96**, 045102 (2017).
- [14] A. Neubauer, J. Bøeuf, A. Bauer, B. Russ, H. v. Löhneysen, and C. Pfleiderer, Ultra-high vacuum compatible image furnace, *Rev. Sci. Instrum.* **82**, 013902 (2011).
- [15] A. Bauer, G. Benka, A. Regnat, C. Franz, and C. Pfleiderer, Ultra-high vacuum compatible preparation chain for intermetallic compounds, *Rev. Sci. Instrum.* **87**, 113902 (2016).
- [16] H. Nielsen and M. Ninomiya, A no-go theorem for regularizing chiral fermions, *Phys. Lett.* **105B**, 219 (1981).
- [17] M.A. Wilde, M. Dodenhöft, A. Niedermayr, A. Bauer, M.M. Hirschmann, K. Alpin, A.P. Schnyder, and C. Pfleiderer, Symmetry-enforced topological nodal planes at the Fermi surface of a chiral magnet, *Nature (London)* **594**, 374 (2021).
- [18] We note that a maximal Chern number  $\pm 2$  is sometimes assigned to points without SOC as opposed to  $\pm 4$  with SOC [4–7]. This difference is somewhat artificial and reflects solely how spin degeneracy is counted and not a fundamental difference of the topological winding (see also Supplemental Material [9]).
- [19] X. Xu, X. Wang, T.A. Cochran, D.S. Sanchez, G. Chang, I. Belopolski, G. Wang, Y. Liu, H.-J. Tien, X. Gui, W. Xie, M.Z. Hasan, T.-R. Chang, and S. Jia, Crystal growth and quantum oscillations in the topological chiral semimetal CoSi, *Phys. Rev. B* **100**, 045104 (2019).
- [20] D.S. Wu, Z.Y. Mi, Y.J. Li, W. Wu, P.L. Li, Y.T. Song, G.T. Liu, G. Li, and J.L. Luo, Single crystal growth and magnetoresistivity of topological semimetal CoSi, *Chin. Phys. Lett.* **36**, 077102 (2019).
- [21] H. Wang, S. Xu, X.-Q. Lu, X.-Y. Wang, X.-Y. Zeng, J.-F. Lin, K. Liu, Z.-Y. Lu, and T.-L. Xia, De Haas–van Alphen quantum oscillations and electronic structure in the large-Chern-number topological chiral semimetal CoSi, *Phys. Rev. B* **102**, 115129 (2020).
- [22] W. Wu, Y. Liu, S. Li, C. Zhong, Z.-M. Yu, X.-L. Sheng, Y.X. Zhao, and S.A. Yang, Nodal surface semimetals: Theory and material realization, *Phys. Rev. B* **97**, 115125 (2018).
- [23] Z.-M. Yu, W. Wu, Y.X. Zhao, and S.A. Yang, Circumventing the no-go theorem: A single Weyl point without surface Fermi arcs, *Phys. Rev. B* **100**, 041118(R) (2019).
- [24] P. Blaha, K. Schwarz, F. Tran, R. Laskowski, G.K.H. Madsen, and L.D. Marks, WIEN2k: An APW + lo program for calculating the properties of solids, *J. Chem. Phys.* **152**, 074101 (2020).
- [25] P. Giannozzi *et al.*, QUANTUM ESPRESSO: A modular and open-source software project for quantum simulations of materials, *J. Phys. Condens. Matter* **21**, 395502 (2009).
- [26] A. Dal Corso, Pseudopotentials periodic table: From H to Pu, *Comput. Mater. Sci.* **95**, 337 (2014).
- [27] J.P. Perdew, K. Burke, and M. Ernzerhof, Generalized Gradient Approximation Made Simple, *Phys. Rev. Lett.* **77**, 3865 (1996).
- [28] T. Fukui, Y. Hatsugai, and H. Suzuki, Chern numbers in discretized Brillouin zone: Efficient method of computing (Spin) Hall conductances, *J. Phys. Soc. Jpn.* **74**, 1674 (2005).
- [29] A.A. Mostofi, J.R. Yates, Y.-S. Lee, I. Souza, D. Vanderbilt, and N. Marzari, Wannier90: A tool for obtaining maximally-localised Wannier functions, *Comput. Phys. Commun.* **178**, 685 (2008).
- [30] G. Pizzi *et al.*, Wannier90 as a community code: New features and applications, *J. Phys. Condens. Matter* **32**, 165902 (2020).
- [31] D. Gosálbez-Martínez, I. Souza, and D. Vanderbilt, Chiral degeneracies and Fermi-surface Chern numbers in bcc Fe, *Phys. Rev. B* **92**, 085138 (2015).
- [32] C. Guo, L. Hu, C. Putzke, J. Diaz, X. Huang, K. Manna, F.-R. Fan, C. Shekhar, Y. Sun, C. Felser, C. Liu, B.A. Bernevig, and P.J.W. Moll, Quasi-symmetry-protected topology in a semi-metal, *Nat. Phys.* (2022); M.A. Wilde and C. Pfleiderer, Large curvature near a small gap, *Nat. Phys.* (2022); These papers consider the putative relevance of quasi symmetries for the Berry curvature.
- [33] D. Shoenberg, *Magnetic Oscillations in Metals* (Cambridge University Press, Cambridge, England, 1984).
- [34] J.Z. Ma *et al.*, Observation of a singular Weyl point surrounded by charged nodal walls in PtGa, *Nat. Commun.* **12**, 3994 (2021).
- [35] J.-Z. Ma, S.-N. Zhang, J.P. Song, Q.-S. Wu, S.A. Ekahana, M. Naamneh, M. Radovic, V.N. Strocov, S.-Y. Gao, T. Qian, H. Ding, K. He, K. Manna, C. Felser, N.C. Plumb, O.V. Yazyev, Y.-M. Xiong, and M. Shi, Giant Chern number of a Weyl nodal surface without upper limit, *Phys. Rev. B* **105**, 115118 (2022).